IEEE Access
Multidisciplinary | Rapid Review | Open Access Journal

Received February 9, 2021, accepted February 26, 2021, date of publication March 2, 2021, date of current version March 10, 2021.

Digital Object Identifier 10.1109/ACCESS.2021.3063120

Multi-Channel-Based Differential Pathlength Factor Estimation for Continuous-Wave fNIRS

RUISEN HUANG, (Graduate Student Member, IEEE), AND KEUM-SHIK HONG, (Fellow, IEEE)
School of Mechanical Engineering, Pusan National University, Busan 46241, South Korea

Corresponding author: Keum-Shik Hong (kshong@pusan.ac.kr)

This work was supported by in part by the China Scholarship Council under Grant 201808260086, and in part by the National Research Foundation (NRF) of South Korea through the auspices of the Ministry of Science and ICT, South Korea, under Grant NRF-2020R1A2B5B03096000.

ABSTRACT Functional near-infrared spectroscopy (fNIRS) in brain imaging needs to be robust to subject-wise variability. The use of a fixed differential pathlength factor (DPF) per wavelength for the entire brain will degrade the accuracy of hemodynamic responses. Since the tissue composition varies within the brain, correct DPF values should be used for various emitter-detector distances and brain regions. In this article, a DPF estimation method combining a state-space model of the modified Beer-Lambert law (mBLL), a parameter model for estimating the reduced scattering coefficients, and dual square-root cubature Kalman filters (SCKFs) is proposed. To validate the proposed method, known light intensities (six channels, two wavelengths) and reference DPFs are generated using NIRFAST (a Matlab toolbox) using a presumed paradigm, known tissue properties, a Balloon model, and a finite element head model consisting of 58,818 mesh elements. Then, the DPF values are estimated using a Jacobian matrix from the head model and the mBLL. The results show that the estimated concentration changes correlate well with the reference data. Also, the estimated DPFs showed relative errors less than 1.33% maximum and 0.75% on average. A one-tailed t-test revealed that the estimated DPFs matched the reference DPFs with more than 99.9% confidence. The developed method can efficiently access the actual DPFs even if emitter-detector distances vary significantly and the tissue properties are not uniform. With the developed state-space models for dual SCKFs, real-time estimation of the DPFs from one experiment to another has become plausible.

INDEX TERMS Differential pathlength factor (DPF), functional near-infrared spectroscopy (fNIRS), Kalman filter, state-space method, finite element method (FEM).

I. INTRODUCTION

The differential pathlength factor (DPF) in optics is defined as a ratio between the total traveling distance of light and the geometric distance between light source and detector on the tissue surface. Once a wavelength is given, the DPF value is assumed constant regardless of tissue properties when the optode spacing is larger than 25 mm [1]. However, the DPF depends on the tissue's composition and micro/macroscopic structures, and underneath blood flow. Also, it varies upon a subject's head locations and across subjects. The misuse of a wrong DPF value may lead to incorrect oxy- and deoxy-hemoglobin (HbO, HbR) concentrations when using the modified Beer-Lambert law (mBLL). Therefore, the correct use of DPF values is essential for an accurate disease diagnosis [2]. This article develops a DPF estimation algorithm for a continuous-wave functional near-infrared spectroscopy system (fNIRS).

The fNIRS is an emerging non-invasive technology for brain imaging, which can substitute functional magnetic resonance imaging (fMRI) in cost, portability, and temporal resolution [3]–[5]. Moreover, it outperforms other modalities like magnetoencephalography (MEG) and electro-encephalography (EEG) regarding spatial resolution. The non-invasiveness and safe nature make it a better daily solution for brain monitoring and supervision than positron emission tomography (PET) [6]–[10]. Portable fNIRS applications require the technology to be robust against subjects' movements and noisy environments so that participants can have a more pleasant experience [11]–[13].

In obtaining hemoglobin concentration changes, various hardware modalities were proposed in the literature: In the continuous wave-type domain, the mBLL [14]–[19] has been extensively used, providing relative hemoglobin

The associate editor coordinating the review of this manuscript and approving it for publication was Ehsan Asadi.

concentration changes. In frequency-domain fNIRS systems, a diffusion approximation of the Boltzmann transport equation has been developed [20]–[22]. In the time-domain, the time-correlated single-photon counting technique has been investigated by researchers [23]. Regarding fNIRS signal processing, many studies argued that, besides the conventional averaging [24], [25], the deconvolution method and an integrated framework method effectively extracted the event-related hemodynamic responses from the overall hemoglobin changes [25], [26]. However, these methods [24]–[26] focused on filtering methods of the hemoglobin signals obtained from optical intensities rather than optical intensities' conversion process to hemoglobin signals.

When the mBLL law is adopted, a priori knowledge of photon-traveling pathlength in the brain becomes critical. Since the real traveling length (unknown) can be approximated by introducing the concept of DPF [27]–[30], numerous studies focused on DPF estimation [31]–[33]. An erroneous DPF can yield an inaccurate estimation of hemodynamic responses (HRs) [33]. Some studies proposed a DPF estimation by an offline Monte-Carlo method [32], [34], [35], while others proposed approaches based on the analysis of a time-domain contrast function for compensation [36], [37]. The Monte-Carlo method assumes that the DPF is identical for all channels, while the latter is only suitable for time-domain fNIRS. The latter proposes the use of an extended Kalman filter for DPF estimation. However, the requirement of using four different wavelengths is limited to its application. Because the method in [33] employed an identity matrix in the state-transition matrix, the estimated hemoglobin concentrations were restricted to slow-varying components.

Several studies recently investigated relative DPFs instead of absolute values, either online or offline: Zhao's group [32] managed to map the DPFs of an adult's forehead using time-domain fNIRS. However, time-domain fNIRS devices are costly and not portable, which limits the application of their method. Scholkmann's group [38] developed a statistical equation for DPFs in terms of age and wavelength for the frontal cortex. The method in [38] is easily applicable, but it ignores the possible differences in DPFs at different brain locations. Moreover, it is applicable only in the frontal cortex, not for the other cortices. Piao's group [39] investigated the geometric dependence of DPFs using simple homogeneous geometric models. Their study gave an insight from the optical view in DPF calculation. Nevertheless, it was not extended to the head model application yet. Chiarelli's group [40] estimated DPFs offline using multi-distance high-density measurements. Their approach was suitable for low-resolution maps of DPFs and could reduce hemoglobin crosstalk due to statistical calculation dominance [40]. Yet, it requires more than twenty channels for one estimation, so that it might lead to a more significant requirement on the hardware.

In this article, we address the fundamental issue in optics, DPF estimation. This article's contributions are i) This is the first work developing an online DPF estimation algorithm using the parameters appearing in the mBLL for continuous-wave type fNIRS systems. ii) Dual state-space models (one for the mBLL and another for the reduced scattering coefficients) are developed for the first time. iii) Simultaneous computation of HRs and DPF estimation can be done without an additional device. iv) The developed method can be applied to all brain regions, not restricted to the prefrontal cortex. The developed two state-space models are incorporated in a dual square-root cubature Kalman filter (SCKF) for online estimation of hemoglobin concentration changes and the DPFs for individual channels. Finally, the proposed work is validated by generating reference DPF values with a Matlab toolbox and comparing them with the estimated ones.

The rest of this article is structured as follows: Section II develops dual state-space models: one for the mBLL and another for the parameters appearing in the mBLL. Also, the theory to establish a dual SCKF is outlined. Section III discusses a validation scheme of the developed method in Section II, in which a Matlab toolbox (NIRFAST) is used. In Section IV, a finite element mesh within NIRFAST, paradigm to generating HRs, and reference DPFs are synthesized. This section also explains the HR generation using the Balloon model and the statistical analysis methods (t-test, correlation analysis, etc.). In Section V, the proposed method's obtained results and those from an extended Kalman filter and a linear regression method are compared. Conclusions are made in Section VI.

II. METHODS AND THEORY

A. STATE-SPACE MODEL

The continuous-wave diffuse reflectance of light can be written using the mBLL [16], [18].

$$I(\lambda, l) = I_0(\lambda) e^{-\mu(\lambda, l)\cdot l \cdot d(\lambda, l) + C}, \tag{1}$$

where λ denotes the wavelength, l denotes the source-detector distance, $I(\lambda, l)$ is the measured light intensity, $I_0(\lambda)$ is the injected light, $\mu(\lambda, l)$ and $d(\lambda, l)$ are the absorption coefficient and the DPF depending on λ and l, respectively, and C is a medium- and geometry-dependent constant.

Consider two wavelengths (λ_1 and λ_2) and two pairs of emitter-detector distances (i.e., l_1 and l_2), in which the same detector measures light emitted from two nearby sources, see Fig. 1. The absorption coefficients change in time as the blood composition changes in time. Let $I(k; \lambda_i, l_j)$ be the measured light intensity of wavelength λ_i ($i = 1, 2$) and distance l_j ($j = 1, 2$) at time k, $I(0; \lambda_i, l_j)$ be the initial light intensity

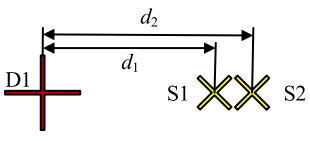

FIGURE 1. Two emitter-detector pairs with close distances.

at time 0, $\alpha_{\mathrm{HbX}}(\lambda_i)$ denote the extinction coefficient of HbX (i.e., HbO or HbR) of wavelength λ_i, $\Delta HbX(k;\, l_j)$ represent the HbX concentration changes of distance l_j at time k (when ΔHbX is computed, both wavelengths are used, and therefore subscript i does not appear); $\mu(k;\, \lambda_i,\, l_j) = \alpha_{\mathrm{HbO}}(\lambda_i)\Delta HbO(k;\, l_j) + \alpha_{\mathrm{HbR}}(\lambda_i)\Delta HbR(k;\, l_j)$ be the absorption coefficients, and $d(k;\, \lambda_i,\, l_j)$ define the differential pathlength factor of wavelength λ_i and distance l_j. For brevity, we simplify the dependence on λ_i and l_j using subscripts i and j as follows; $I_{i,j}(k) = I(k;\, \lambda_i,\, l_j)$, $\Delta HbX_j(k) = \Delta HbX(k;\, l_j)$, $\mu_{i,j}(k) = \mu(k;\, \lambda_i,\, l_j)$, and $d_{i,j}(k) = d(k;\, \lambda_i,\, l_j)$.

The optical density (or absorbance) equations for two wavelengths and two distances are obtained as follows [16].

$$-\ln\frac{I_{i,j}(k)}{I_{i,j}(0)} = \left(\alpha_{\mathrm{HbO}}(\lambda_i)\Delta HbO_j(k) + \alpha_{\mathrm{HbR}}(\lambda_i)\Delta HbR_j(k)\right) \cdot l_j \cdot d_{i,j}(k)\ \mu_{i,j}(k) \cdot l_j \cdot d_{i,j}(k), \tag{2}$$

where $\mu_{i,j}(k) = \alpha_{\mathrm{HbO}}(\lambda_i)\Delta HbO_j(k) + \alpha_{\mathrm{HbR}}(\lambda_i)\Delta HbR_j(k)$ for $i = 1, 2$ and $j = 1, 2$. Let the state vector $x \in R^4$ be defined as follows.

$$x(k) = \left[\ \Delta HbO_1(k)\ \ \Delta HbR_1(k)\ \ \Delta HbO_2(k)\ \ \Delta HbR_2(k)\ \right]^T, \tag{3}$$

where subscripts 1 and 2 denote distances l_1 and l_2. Equation (2) can be rewritten in the state-space form employing an identity process and a measurement vector $y(k) \in R^4$.

$$x(k) = x(k-1) + n_1, \tag{4}$$
$$y(k) = H(\phi)x(k) + v_1, \tag{5}$$

where

$$y(k) = -\left[\ \ln\frac{I_{1,1}(k)}{I_{1,1}(0)}\ \ln\frac{I_{2,1}(k)}{I_{2,1}(0)}\ \ln\frac{I_{1,2}(k)}{I_{1,2}(0)}\ \ln\frac{I_{2,2}(k)}{I_{2,2}(0)}\ \right]^T, \tag{6}$$

and $H(\cdot)$ is defined in (7), as shown at the bottom of the next page. n_1 and v_1 are noises, and the DPF $d_{i,j}(k)$ has been specified as a function of an unknown parameter vector ϕ consisting of the reduced scattering coefficients at distance l_j.

On the other hand, the light exponential attenuation rate of (1) caused by the interaction of absorption and diffusion can be quantified using the effective absorption coefficient $\mu_{\mathrm{eff}}(\lambda,\, l)$ as

$$I(\lambda,\, l) = I_0(\lambda)e^{-\mu_{\mathrm{eff}}(\lambda,\, l)\cdot l + C}. \tag{8}$$

Also, the effective absorption coefficient is calculated as

$$\mu_{\mathrm{eff}}(\lambda,\, l) = \sqrt{3\mu(\lambda,\, l)\left(\mu(\lambda,\, l) + \mu'(\lambda)\right)}, \tag{9}$$

where $\mu'(\lambda)$ is the reduced scattering coefficients, see Eq. (17) in [40]. In our four cases, the DPFs can be computed as follows, see [40, eq. (9)].

$$d_{i,j}(k) = \frac{\partial\mu_{\mathrm{eff}}(k;\, \lambda_i,\, l_j)}{\partial\mu_{i,j}(k)} = \frac{3(2\mu_{i,j}(k) + \mu_i')}{2\sqrt{3\mu_{i,j}(k)(\mu_{i,j}(k) + \mu_i')}} = \frac{3(2\mu_{i,j}(k) + \mu_i')}{2\mu_{\mathrm{eff}}(\lambda_i,\, d_j)}, \tag{10}$$

where $\mu_{\mathrm{eff}}(k;\, \lambda_i,\, l_j) = \sqrt{3\mu_{i,j}(k)(\mu_{i,j}(k) + \mu_i')}$. It is noted that the reduced scattering coefficient μ_i' (i.e., $\mu'(\lambda_i)$) depends on the composition of a subject's brain tissues (the variation of μ_i' for a small distance difference between l_1 and l_2 has been ignored), which is now considered as a parameter appearing in $d_{i,j}(k)$. Let ϕ be the parameter vector consisting of two reduced scattering coefficients as follows.

$$\phi = \left[\ \mu_1'\ \ \mu_2'\ \right]^T, \tag{11}$$

where the subscripts 1 and 2 denote the wavelengths. Using the state variables in (3) and unknown parameters in (11), (10) is rewritten as follows.

$$d_{i,j}(k) = d_{i,j}\left(x(k),\, \phi\right) = \frac{3\left(2\mu_{i,j}(x(k)) + \mu_i'\right)}{2\mu_{\mathrm{eff}}(x(k),\, \phi)}. \tag{12}$$

Based on the transport equation's diffusion approximation, the following relations between the effective absorption coefficients and source-detector distances hold [41].

$$\ln\left(I_{i,j}(k)\cdot l_j\right) = l_j\frac{\sum_{j=1}^{2}\mu_{\mathrm{eff}}(\lambda_i,\, l_j)}{2} + C_1. \tag{13}$$

For a given wavelength λ_i, two measurement data for l_1 and l_2 can be combined into one equation.

$$\ln\left(I_{i,1}(k)/I_{i,2}(k) + \tau_i\right) = (l_2 - l_1)\,\mu_{\mathrm{eff}}(\lambda_i) - 2\cdot\ln(l_1/l_2), \tag{14}$$

where τ_1 and τ_2, obtained by preliminary phantom experiments, are the calibration constants of experimental data. Therefore, a second state-space model for estimating ϕ is introduced as follows.

$$\phi(k) = \phi(k-1) + n_2, \tag{15}$$
$$\psi(k) = g\left(x(k),\, \phi(k)\right) + v_2, \tag{16}$$

where

$$\psi(k) = \begin{bmatrix}\ln\left(I_{1,1}(k)/I_{1,2}(k) + \tau_1\right)\\ \ln\left(I_{2,1}(k)/I_{2,2}(k) + \tau_2\right)\end{bmatrix}, \tag{17}$$

$$g(x(k),\, \phi(k)) = \begin{bmatrix}(l_2 - l_1)\,\mu_{\mathrm{eff}}(\lambda_1) - 2\cdot\ln\frac{l_1}{l_2}\\ (l_2 - l_1)\,\mu_{\mathrm{eff}}(\lambda_2) - 2\cdot\ln\frac{l_1}{l_2}\end{bmatrix}. \tag{18}$$

Now, Fig. 2 summarizes all the development above, which includes two state-space models: One for the mBLL and another for the unknown parameters appearing in the mBLL (i.e., the reduced scattering coefficients). For these two models, a dual square-root cubature Kalman filter (SCKF) is developed in the next section.

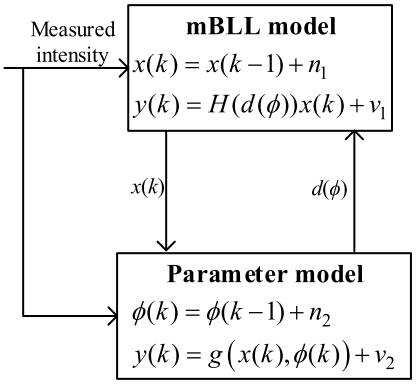

where

$$x = \begin{bmatrix} \Delta HbO_1 \\ \Delta HbR_1 \\ \Delta HbO_2 \\ \Delta HbR_2 \end{bmatrix}, \quad \phi = \begin{bmatrix} \mu_1' \\ \mu_2' \end{bmatrix},$$

$$d(\phi) = \frac{3(2\mu + \mu')}{2\mu_{\text{eff}}}, \quad \mu_{\text{eff}} = \sqrt{3\mu(\mu + \mu')},$$

$$\mu = \alpha_{\text{HbO}} \Delta HbO + \alpha_{\text{HbR}} \Delta HbR,$$

$H(d)$ in (7), and $g(x, \phi)$ in (18).

FIGURE 2. The proposed dual-model scheme for estimating differential pathlength factors: mBLL and the reduced scattering coefficients.

B. DUAL KALMAN FILTER

The SCKF is a filter for estimating nonlinear models [42], [43]. The filter approximates the integration of the product of a nonlinear function and its likelihood density, which is usually approximated by the Gaussian, using the spherical-radial cubature rule or spherical simplex-radial cubature rule [44]–[48].

The dimensions of two models (4)-(7) and (15)-(18) are $m = 4$ and $m = 2$, respectively. Let e_i be the ith column vector of the m-dimensional identity matrix E_m. According to the 3rd-order spherical-radial cubature rule, the new sampling points ξ_i $(1 \le i \le m)$ after nonlinear transform and their weights w_i are defined as follows.

$$\begin{aligned} \xi_i &= \vartheta + \sqrt{mP} e_i = \vartheta + \sqrt{m} S e_i, \\ w_i &= \frac{1}{2m}, \\ \xi_{i+m} &= \vartheta - \sqrt{mP} e_i = \vartheta - \sqrt{m} S e_i, \\ w_{i+m} &= \frac{1}{2m}, \end{aligned} \tag{19}$$

where ϑ is the mean of the new sampling points. P is the error covariance matrix of the process equation, which should be non-negative definite so that its square-root matrix, S, exists.

The filter assumes that the noises in the process equations of (4) and (15), n_1 and n_2, observe Gaussian distribution averaging at q_1 and q_2, i.e., $n_1 \sim \aleph(q_1, Q_1)$, and $n_2 \sim \aleph(q_2, Q_2)$. Q_i, $(i = 1 \text{ or } 2)$ is the error covariance matrix for n_i. Similarly, the noises in the measurement equations (5) and (16), v_1 and v_2, satisfy $v_1 \sim \aleph(r_1, R_1)$, and $v_2 \sim \aleph(r_2, R_2)$, where r_1 and r_1 are the means of v_1 and v_2, and R_i $(i = 1 \text{ or } 2)$ is the error covariance matrix for v_i.

Introducing the SCKF structure, let $\phi_r(k)$ and x_r be the reference parameter vector and the reference state vector, respectively. Let the variables with a hat denote the estimated values. Let $S_\phi(k)$ and $S_x(k)$ be the square-root error covariance matrices for the parameter vector and the state vector, respectively. Initializing the states, we have

$$\begin{aligned} \hat{\phi}(0) &= E[\phi], S_\phi(0) = \sqrt{E\left[\left(\phi_r - \hat{\phi}(0)\right)\left(\phi_r - \hat{\phi}(0)\right)^T\right]}, \\ \hat{x}(0) &= E[x], S_x(0) = \sqrt{E\left[\left(x_r - \hat{x}(0)\right)\left(x_r - \hat{x}(0)\right)^T\right]}. \end{aligned} \tag{20}$$

In the time update process, the cubature sample points can be computed using (19) with $\vartheta = \hat{x}$ $(k\text{-}1)$ and $S = S_x(0)$. Then, the prior estimation of the state vector, $X_i(k|\ k\text{-}1)$, yields

$$X_i(k|k-1) = f(\xi_i) + q_j, \quad j = 1 \text{ or } 2, \tag{21}$$

where the function $f(x) = x$ according to Section A for both state-space models, and the means of the noises in the process equations are q_1 and q_2, respectively. Therefore, the prior estimate of the state vector becomes

$$\hat{x}(k|k-1) = \sum_{i=1}^{2m} w_i \cdot X_i^*(k|k-1), \tag{22}$$

where

$$\begin{aligned} X^*(k|k-1) &= \begin{bmatrix} X_1^*(k|k-1) \\ \vdots \\ X_{2m}^*(k|k-1) \end{bmatrix} \\ &= \begin{bmatrix} \sqrt{w_1}(X_1(k|k-1) - \hat{x}(k|k-1)) \\ \vdots \\ \sqrt{w_{2m}}(X_{2m}(k|k-1) - \hat{x}(k|k-1)) \end{bmatrix}^T, \end{aligned} \tag{23}$$

and let $X_i^*(k|k-1) = \sqrt{w_i}(X_i(k|k-1) - \hat{x}(k|k-1))$, $i \in \{1, 2, \ldots, 2m\}$. Let $S_Q(k)$ be the square-root matrix of $Q(k)$, N and M be the QR decomposition of a matrix, and

$$H(\phi) = \begin{bmatrix} \alpha_{\text{HbO}}(\lambda_1) l_1 d_{1,1}(\phi) & \alpha_{\text{HbR}}(\lambda_1) l_1 d_{1,1}(\phi) & 0 & 0 \\ \alpha_{\text{HbO}}(\lambda_2) l_1 d_{2,1}(\phi) & \alpha_{\text{HbR}}(\lambda_2) l_1 d_{2,1}(\phi) & 0 & 0 \\ 0 & 0 & \alpha_{\text{HbO}}(\lambda_1) l_2 d_{1,2}(\phi) & \alpha_{\text{HbR}}(\lambda_1) l_2 d_{1,2}(\phi) \\ 0 & 0 & \alpha_{\text{HbO}}(\lambda_2) l_2 d_{2,2}(\phi) & \alpha_{\text{HbR}}(\lambda_2) l_2 d_{2,2}(\phi) \end{bmatrix}, \tag{7}$$

$S(k|k-1)$ be the square-root matrix of the error covariance matrix. Then, $S_x(k|k-1)$ can be computed as follows.

$$[N, M] = \mathrm{qr}\left(\left[X^*(k|k-1)\ S_Q(k-1)\right]^T\right), \quad (24)$$

$$S_x(k|k-1) = M(1:m,:)^T, \quad (25)$$

where M is an upper triangular matrix and $M(1{:}\,m,:)$ denotes M's first m rows and qr denotes the QR decomposition. The measurement update gives a posterior estimation of the state vector based on the prior estimate and the measurement equations. Similarly, the cubature sample points are recalculated using the prior estimate and the prior error covariance matrix, i.e., $\vartheta = \hat{x}\ (k|k\text{-}1)$ and $S = S_x(k|k\text{-}1)$ for (19).

The prior estimate of the measurement vector yields

$$\hat{z}(k|k-1) = \sum_{i=1}^{m} w_i \left(h(\xi_i) + r_j\right), \quad j = 1 \text{ or } 2, \quad (26)$$

where the function $h(\cdot)$ is the measurement equation in the model. For the mBLL model, $h(\cdot)$ corresponds to the measurement equations (5)-(7). As for the parameter model, $h(\cdot)$ represents equations (16)-(18). The variables, r_1 and r_2, are the means of noises in the measurement equations.

Let $S_R(k)$ be the square-root matrix of R_i, $i = 1$ or 2. Similar to (24) and (25), the square-root innovation covariance matrix, S_{zz}, can be calculated as

$$[N, M] = \mathrm{qr}\left(\left[Z^*(k|k-1)\ S_R(k)\right]^T\right), \quad (27)$$

$$S_{zz}(k|k-1) = M\ (1:m,:)^T, \quad (28)$$

where M is an upper triangular matrix and $M(1{:}\,m,:)$ denotes M's first m rows. Then, $Z^*(k|k\text{-}1)$ can be defined as

$$Z^*(k|k-1) = \begin{bmatrix} \sqrt{w_1}\left(h(\xi_1) - \hat{z}(k|k-1)\right) \\ \vdots \\ \sqrt{w_{2m}}\left(h(\xi_{2m}) - \hat{z}(k|k-1)\right) \end{bmatrix}^T. \quad (29)$$

With (29), the cross-covariance matrix of the state vector and the measurement vector, $P_{xz}(k|k\text{-}1)$, yields

$$P_{xz}(k|k-1) = X'(k|k-1)Z^*(k|k-1)^T, \quad (30)$$

where

$$X'(k|k-1) = \begin{bmatrix} \sqrt{w_1}\left(\xi_1 - \hat{x}(k|k-1)\right) \\ \vdots \\ \sqrt{w_{2m}}\left(\xi_{2m} - \hat{x}(k|k-1)\right) \end{bmatrix}. \quad (31)$$

Then, from (28) and (30), we obtain the Kalman gain, $G(k)$, as

$$G(k) = \left(P_{xz}(k|k-1)/S_{zz}(k|k-1)^T\right)/S_{zz}(k|k-1). \quad (32)$$

The posterior estimate of the state vector will be

$$\hat{x}(k) = \hat{x}(k|k-1) + G(k)\left(z(k) - \hat{z}(k|k-1)\right). \quad (33)$$

According to (29), (31), and (32), the posterior estimate of the square-root error covariance matrix, $S(k)$, is computed as follows.

$$S(k)^T = qr\left(\left[X'(k|k-1) - G(k)Z^*(k|k-1)\ G(k)S_R(k)\right]^T\right). \quad (34)$$

The SCKF can improve the estimation accuracy for a highly nonlinear model compared to the extended Kalman filter and the unscented Kalman filter. We take two SCKFs for the state estimation and the DPF estimation, respectively [49]. The alternate estimate between the filters enables a more accurate estimate and less computational demand.

III. VALIDATAION OF DPF ESTIMATION METHOD

Fig. 3 depicts a schematic to validate the proposed DPF estimation method developed in Section II, using NIRFAST (a Matlab toolbox) [56]. Validation is done by comparing the estimated DPF values obtained through the DSCKF and the known DPF values (in this article, the known DPF values are computed using the absorption and reduced scattering coefficients obtained from NIRFAST). NIRFAST can generate an FEM mesh to provide solutions to two problems (forward and inverse). The forward problem solves the light transport equation [56] for photon densities when a 3D FEM mesh, the absorption coefficient, the diffusion coefficient, and an input (light source) are provided. On the other hand, the inverse problem results in the absorption and scattering coefficients through the Levenberg-Marquardt algorithm for given optical densities and an FEM mesh.

In this article, the hemodynamic responses are first synthesized as a weighted sum of the canonical HR from the Balloon model and the physiological noise (i.e., $\Delta HbX = a{\cdot}HR + b \cdot n_{\mathrm{phys}}$). Also, a 3D head mesh is generated to solve the light transport equation. Then, for given ΔHbX and a 3D mesh, NIRFAST generates the light intensities (forward solution with assumed initial reduced scattering coefficients) and the absorption and reduced scattering coefficients of individual channels (inverse problem). The absorption and reduced scattering coefficients are then used to compute the DPFs (the upper part in Fig. 3). On the other hand, the same light intensities obtained from NIRFAST are used in the estimation of the DPFs using the proposed DSCKF scheme (the lower part in Fig. 3).

The estimation results will be verified from two aspects. First, the estimated concentration changes (i.e., $\hat{x}$) are compared with the reconstructed ones in NIRFAST. Both signals (estimated, reconstructed) are low-pass-filtered by a fourth-order low-pass Butterworth filter with a cutoff frequency of 0.15 Hz. The correlation coefficients between the two signals are examined. Second, the trend of estimation errors is examined. The average relative errors (i.e., $(d_{\mathrm{ref}} - d_{\mathrm{est}})/d_{\mathrm{ref}}$) for four channels are examined too. By examining the maximal and average relative errors, we can evaluate the performance of the proposed method. A one-tailed t-test is to be performed too.

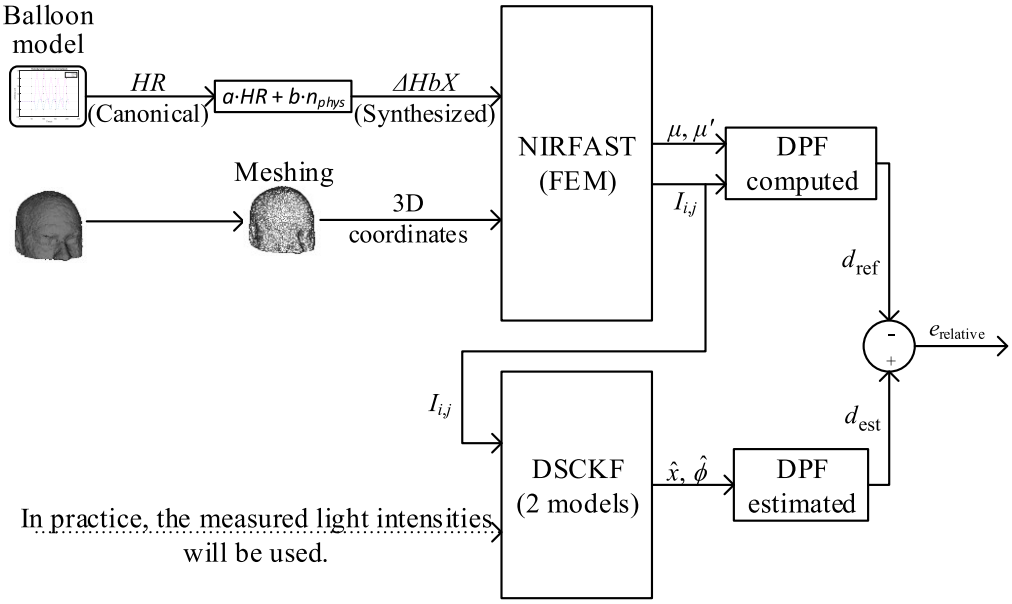

FIGURE 3. Validation of the proposed DSCKF scheme using NIRFAST.

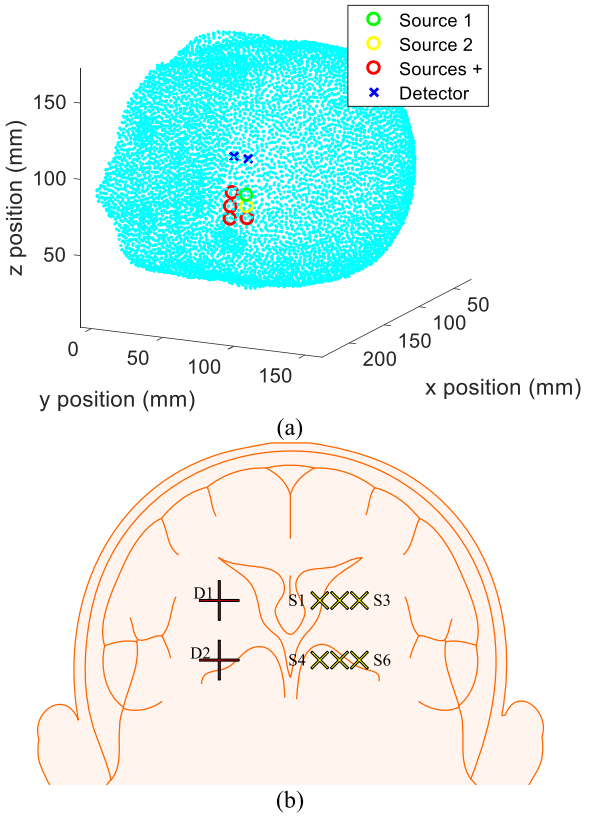

FIGURE 4. 3D FEM meshes generated by NIRFAST [50], [51] and optical topology: (a) The specified optodes' positions within the mesh, (b) the detector-emitter configuration used in the forehead.

IV. NUMERICAL SIMULATION

We simulate the fNIRS process using a subject's forehead FEM model [50], [51]. The Matlab toolbox, NIRFAST, was used.

A. FEM MESH AND OPTICAL TOPOLOGY

Fig. 4a shows a 3-dimensional head model reconstructed from an fMRI image using the NIRFAST [50], [51], consisting of 58,818 tetrahedrons of size 3.5 mm. We can use a finer mesh at the cost of longer computational time. The current mesh size is sufficient to approximate the fNIRS channels' real tissue properties. The shortest channel D1-S1 corresponds to eight tetrahedrons in the mesh. Two detectors (D1, D2) and six sources (S1 to S6) were placed at the model's forehead, see Fig. 4b. The distances of individual source-detector pairs are listed in Table 1. Any two detector-source pairs in a neighborhood can form the two channels for estimating DPFs in Section II. The estimated DPFs will vary upon detector-source distances. The initial chromophores' concentration values adopted for simulation are collected in Table 2.

TABLE 1. Detector-source distance (unit: cm).

	D1	D2
S1	2.31	2.59
S2	3.02	3.27
S3	3.80	4.03
S4	2.37	2.31
S5	3.23	3.19
S6	4.03	4.00

Note: Channels D1-S1, D1-S2, D1-S3, D2-S4, D2-S5, and D2-S6 were used for DPF estimation.

B. HR PARADIGM

The designed paradigm consisted of a two-minute rest at the beginning and five brain activities of 30 seconds (10-sec task, 20-sec rest). A boxcar function was used

TABLE 2. Initial concentrations of the chromophores used in simulation [51].

Molar concentrations (mM)	HbO	HbR	Water
Skin	0.45×10^{-2}	0.15×10^{-2}	0.50
Bone	0.39×10^{-2}	0.98×10^{-3}	0.15
CSF[a]	0.90×10^{-4}	0.10×10^{-4}	0.99
Brain	0.54×10^{-2}	0.22×10^{-2}	0.78

[a]CSF denotes the cerebral spinal fluid layer.

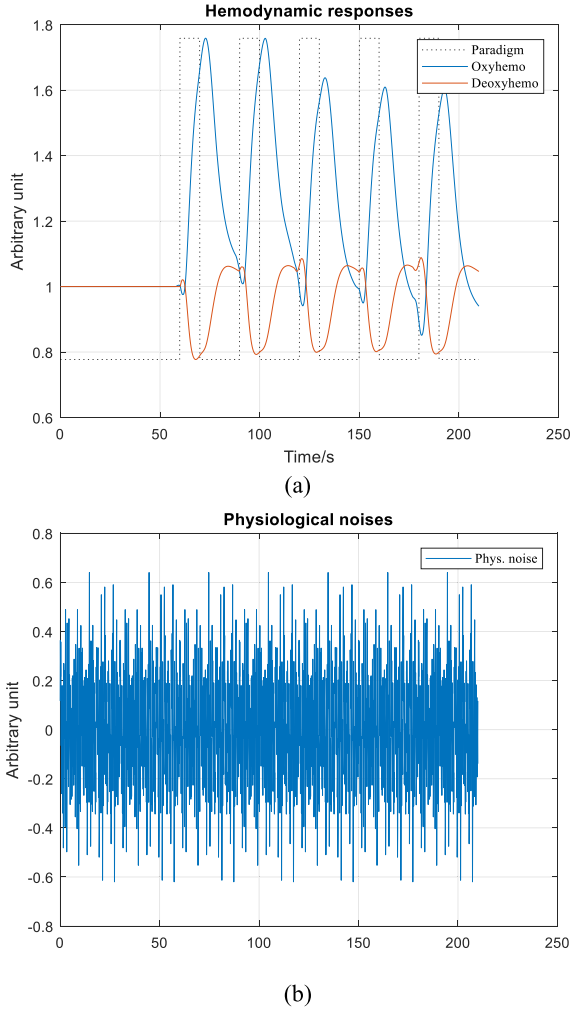

FIGURE 5. Synthesized HRs: (a) The designed paradigm of ΔHbX, (b) the physiological noise.

to describe the stimulation paradigm. The corresponding hemodynamic responses were obtained by solving the Balloon model [52]–[55]. The generated results are shown in Fig. 5a. The physiological noises in Fig. 5b include the cardiac signal and the respiratory signal: The frequency for cardiac noises was 1.17 Hz (70 beats per minute) and that for respiration noises was 0.267 Hz (16 times per minute). After multiplied by a scalar, the noises were linearly added to the pure hemodynamic responses. We used the synthesized

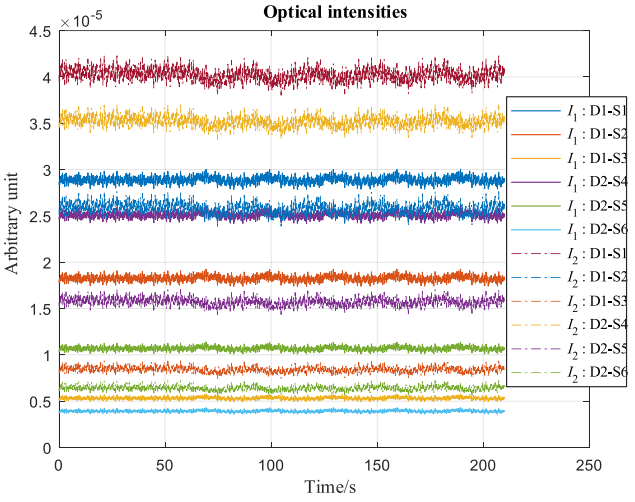

FIGURE 6. Synthesized HRs: (a) The designed paradigm of ΔHbX, (b) the physiological noise.

signals to mimic the brain molar concentrations in the FEM analysis and obtained the corresponding light intensities for individual channels, see Fig. 6.

C. REFERENCE DPF

The chromophore concentrations were reconstructed using the Jacobian matrix, i.e., the weight or sensitivity matrix, J, using the update equation [56]

$$\Delta HbX(k; l_j) = J^T \left(JJ^T + \lambda E\right)^{-1} \cdot OD_{i,j}(k), \qquad (35)$$

where $\Delta HbX(k; l_j) = [\Delta HbO(k; l_j); \Delta HbR(k; l_j)]^{\mathrm{T}}$ denote the chromophore molar concentration changes, E is the identity matrix, and $OD_{i,j}(k) = -\ln(I_{i,j}(k)/I_{i,j}(0))$ $(i, j = 1$ or $2)$ are the optical densities [56]. Since we have $\Delta HbX(k; l_j)$, l_j, and $OD_{i,j}(k)$, where $i, j = 1$ or 2, according to (2), the reference DPFs were calculated as follows.

$$d_{i,j} = \frac{-OD_{i,j}(k)}{\left(l_j \cdot \left(\alpha_{\mathrm{HbO}}(\lambda_i)\Delta HbO_j(k) + \alpha_{\mathrm{HbR}}(\lambda_i)\Delta HbR_j(k)\right)\right)}, \qquad (36)$$

where $j = 1$ or 2 denotes different wavelengths, and l_j distinguishes the detector-source distances. The least-square estimation was used to determine the statistical best fit of the DPFs for all time instances.

V. RESULTS

The estimated concentration changes for D1-S2 and D1-S3 channels are shown in Fig. 7a. The estimation results maintain a similar trend of the reference concentration changes, yet their amplitudes vary slightly. Besides, a small bias is seen in HbR changes for both distances. In Table 3, the correlation coefficients between estimated HRs and reference HRs (from 45 sec to the end) are collected, which shows a high correlation between two signals. The DPF estimation errors

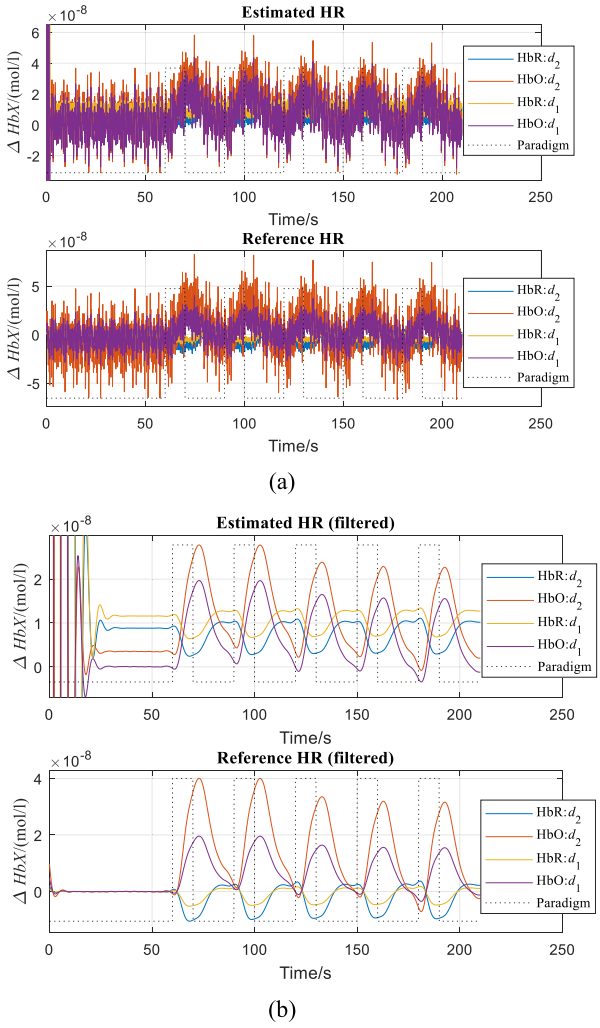

FIGURE 7. Estimated HRs using the proposed DSCKF (simulation results): (a) Estimated HRs (channels D1-S2, D1-S3), (b) low-pass filtered HRs of (a).

TABLE 3. Correlation coefficients between estimated and reference HRs.

	D1-S1 & D1-S2	D1-S2 & D1-S3	D2-S4 & D2-S5	D2-S5 & D2-S6
$\Delta HbO(l_1)$	1.00000	1.00000	0.99998	0.99999
$\Delta HbR(l_1)$	0.99997	0.99989	0.99991	0.99980
$\Delta HbO(l_2)$	1.00000	1.00000	1.00000	1.00000
$\Delta HbR(l_2)$	1.00000	1.00000	1.00000	1.00000

for all channels are shown in Fig. 8. The relative errors in percentage were calculated as follows.

$$e_{\text{relative}} = \frac{d_{\text{est}} - d_{\text{ref}}}{d_{\text{ref}}} \times 100. \tag{37}$$

The relative errors for four detector-source combinations are below 2%.

Similar to the correlation analysis, we analyze the average, variance, and the maxima/minima of the estimation errors.

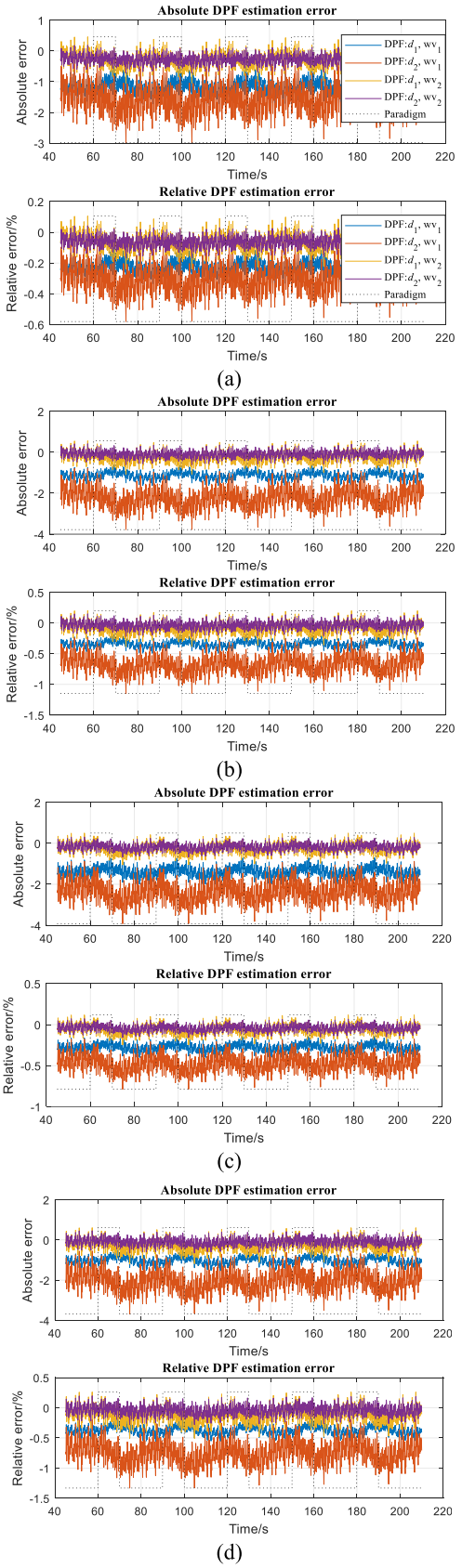

FIGURE 8. Absolute and relative errors of DPF estimation: (a) D1-S1 & D1-S2, (b) D1-S2 & D1-S3, (c) D2-S4 & D2-S5, (d) D2-S5 & D2-S6.

TABLE 4. Relative errors (%) of DPF estimation.

		D1-S1 & D1-S2	D1-S2 & D1-S3	D2-S4 & D2&S5	D2-S5 & D2-S6
Average ± standard deviation	$d_{1,1}$	-0.22± 0.04	-0.34± 0.05	-0.28± 0.05	-0.37± 0.07
	$d_{1,2}$	-0.31± 0.09	-0.69± 0.15	-0.48± 0.10	-0.75± 0.18
	$d_{2,1}$	-0.06± 0.06	-0.08± 0.09	-0.06± 0.06	-0.11± 0.12
	$d_{2,2}$	-0.06± 0.04	-0.03± 0.06	-0.04± 0.04	-0.04± 0.08
Max.	$d_{1,1}$	-0.10	-0.19	-0.14	-0.18
	$d_{1,2}$	-0.04	-0.24	-0.18	-0.20
	$d_{2,1}$	0.11	0.20	0.12	0.26
	$d_{2,2}$	0.04	0.15	0.07	0.20
Min.	$d_{1,1}$	-0.34	-0.49	-0.40	-0.56
	$d_{1,2}$	-0.58	-1.15	-0.79	-1.33
	$d_{2,1}$	-0.24	-0.38	-0.25	-0.51
	$d_{2,2}$	-0.17	-0.22	-0.16	-0.28
p-value	$d_{1,1}$	<0.001	<0.001	<0.001	<0.001
	$d_{1,2}$	<0.001	<0.001	<0.001	<0.001
	$d_{2,1}$	<0.001	<0.001	<0.001	<0.001
	$d_{2,2}$	<0.001	<0.001	<0.001	<0.001
t-value	$d_{1,1}$	-232.34	-100.20	-193.54	-60.90
	$d_{1,2}$	-84.32	62.93	-9.28	65.46
	$d_{2,1}$	-385.35	-225.09	-370.16	-155.36
	$d_{2,2}$	-518.96	-409.37	-564.97	-308.53

The details are listed in Table 4. The maximum average relative error of 0.75% was seen at the D2-S5 and D2-S6 channels. Also, the largest bias of 1.33% occurred from the same combination.

A one-tailed t-test was conducted to compare the relative errors to 0.5%. The results show that the relative errors are mostly below 0.5%, with a confidence of more than 99.9%. The relative DPF errors of 830 nm for D1-S3 and D2-S6 channels were two exceptions (their t-values are positive). However, when analyzed with a threshold of 1%, the t-values of the two pairs turned out to be -81.28 and −49.44, meaning the relative errors were below 1%. Therefore, our proposed method can efficiently evaluate the DPFs for each detector-source pair combination in a neighborhood.

VI. DISCUSSION

This article presented an estimation method of the differential pathlength factor in fNIRS systems using dual square-root cubature Kalman filters (DSCKF) and a multi-distance optical model. Two nearby channels for estimation were taken into account, and an optical model was introduced in the solver to extract the time-of-flight information from measurement data. Inspired by [33], the DSCKF was chosen to incorporate the mBLL and the optical model. While the authors of [33] managed to estimate the relative changes of DPFs, aided by preliminary experiment and calibration on a phantom, the proposed method could efficiently estimate the absolute DPF values.

The proposed method requires no extra hardware like one more wavelength [32] or FD-fNIRS [41]. A carefully designed optodes topology is sufficient. Additionally, when the initial absorption coefficient, μ_{a0}, is calibrated carefully, the estimation results may enable an estimation of the absolute chromophore concentrations as well. Although the SCKF was often used in the industry [57], [58], this is the first application in the fNIRS field. The study's novelty is the proposed state-space models based on the multi-distance optical model and mBLL and the continuous estimation of DPFs using only two nearby channels.

In this article, the use of dual SCKFs for DPF estimation and its mBLL + multi-distance optical model-based state-space model was first proposed. The method allows the continuous estimation of DPF without any limit of the brain location. Talukdar's group succeeded in the continuous correction of DPF but not estimating its actual value [33]. Furthermore, their method is limited to the prefrontal cortex because their reference DPF was only valid for the prefrontal cortex. Chiarelli's group proposed a sophisticated method for DPF estimation [40]. However, their method is feasible for offline analysis instead of continuous estimation. Also, their reference estimation was established upon a multi-channel solution requiring at least 20 channels, which significantly limits its spatial resolution. From these two views, the proposed method is much reliable.

The proposed method can achieve a relative estimation error of less than 1% statistically. Talukdar's group can only provide a continuous correction of the DPFs. Additionally, Chiarelli's group can achieve a relative error ranging between 1% and 4% depending on the integration time windows [40]. It means the proposed method is more suitable for continuous estimation with higher accuracy.

Regarding the complexity of the SCKF algorithm, studies have proven that the complexity of an SCKF-related algorithm has an order between $O(n^2)$ [59] and $O(n^3)$ [60]. However, the variable n here denotes the dimension of the states. In our proposed method, the state vector's dimension is 4, which means the algorithm's corresponding complexity will not exceed $O(64)$. It is affordable for a real-time system.

One of the proposed method's limitations is that the measurement compensations τ_1 and τ_2 in (14) need to be tuned carefully. Inappropriate compensation may lead to significant bias in the results. A solution to the problem is to calibrate τ_1 and τ_2 using a phantom with known optical properties.

VII. CONCLUSION

In this article, a dual SCKF incorporating mBLL and the multi-distance optical model was presented for DPF estimation from fNIRS data. The proposed method enables a higher resolution and continuous estimation. The estimation of the DPFs required only two channels in the neighborhood. During the initialization process, a preliminary experiment on phantom is needed to carefully calibrate the measured data, i.e., constants τ_1 and τ_2 in (14). The estimation results show

that our method can achieve a DPF estimation with a relative error of 1.33% at the maximum at statistical confidence of over 99.9%. The estimated chromophore concentration changes were also well correlated to the actual values. The study provides a new way for continuous DPF estimation and correction and gives the real-time estimation of absolute concentrations in future fNIRS systems.

REFERENCES

[1] M. Essenpreis, M. Cope, C. E. Elwell, S. R. Arridge, P. van der Zee, and D. T. Delpy, "Wavelength dependence of the differential pathlength factor and the log slope in time-resolved tissue spectroscopy," in *Optical Imaging of Brain Function and Metabolism* (Advances in Experimental Medicine and Biology), vol. 333, U. Dirnagl, A. Villringer, K. M. Einhaupl, Eds. Boston, MA, USA: Springer, 1993.

[2] A. J. Lin, A. Ponticorvo, A. J. Durkin, V. Venugopalan, B. Choi, and B. J. Tromberg, "Differential pathlength factor informs evoked stimulus response in a mouse model of Alzheimer's disease," *Neurophotonics*, vol. 2, no. 4, Oct. 2015, Art. no. 045001.

[3] M. A. Yaqub, S.-W. Woo, and K.-S. Hong, "Compact, portable, high-density functional near-infrared spectroscopy system for brain imaging," *IEEE Access*, vol. 8, pp. 128224–128238, 2020.

[4] M. A. Tanveer, M. J. Khan, M. J. Qureshi, N. Naseer, and K.-S. Hong, "Enhanced drowsiness detection using deep learning: An fNIRS study," *IEEE Access*, vol. 7, pp. 137920–137929, 2019.

[5] Z. Sun, Z. Huang, F. Duan, and Y. Liu, "A novel multimodal approach for hybrid brain–computer interface," *IEEE Access*, vol. 8, pp. 89909–89918, 2020.

[6] K.-S. Hong and M. J. Khan, "Hybrid brain–computer interface techniques for improved classification accuracy and increased number of commands: A review," *Frontiers Neurorobot.*, vol. 11, Jul. 2017, Art. no. 35.

[7] N. Naseer and K.-S. Hong, "fNIRS-based brain-computer interfaces: A review," *Frontiers Hum. Neurosci.*, vol. 9, Jan. 2015, Art. no. 3.

[8] J. R. Mansfield, M. G. Sowa, J. R. Payette, B. Abdulrauf, M. F. Stranc, and H. H. Mantsch, "Tissue viability by multispectral near infrared imaging: A fuzzy C-means clustering analysis," *IEEE Trans. Med. Imag.*, vol. 17, no. 6, pp. 1011–1018, Dec. 1998.

[9] F. Scholkmann, S. Kleiser, A. J. Metz, R. Zimmermann, J. M. Pavia, U. Wolf, and M. Wolf, "A review on continuous wave functional near-infrared spectroscopy and imaging instrumentation and methodology," *NeuroImage*, vol. 85, pp. 6–27, Jan. 2014.

[10] X.-S. Hu, K.-S. Hong, and S. S. Ge, "FNIRS-based online deception decoding," *J. Neural Eng.*, vol. 9, no. 2, Apr. 2012, Art. no. 026012.

[11] I. Miyai, H. C. Tanabe, I. Sase, H. Eda, I. Oda, I. Konishi, Y. Tsunazawa, T. Suzuki, T. Yanagida, and K. Kubota, "Cortical mapping of gait in humans: A near-infrared spectroscopic topography study," *NeuroImage*, vol. 14, no. 5, pp. 1186–1192, Nov. 2001.

[12] S. Perrey, "Non-invasive NIR spectroscopy of human brain function during exercise," *Methods*, vol. 45, no. 4, pp. 289–299, Aug. 2008.

[13] M. N. A. Khan, M. R. Bhutta, and K.-S. Hong, "Task-specific stimulation duration for fNIRS brain-computer interface," *IEEE Access*, vol. 8, pp. 89093–89105, 2020.

[14] S. Srinivasan, B. W. Pogue, S. Jiang, H. Dehghani, C. Kogel, S. Soho, J. J. Gibson, T. D. Tosteson, S. P. Poplack, and K. D. Paulsen, "Interpreting hemoglobin and water concentration, oxygen saturation, and scattering measured *in vivo* by near-infrared breast tomography," *Proc. Nat. Acad. Sci. USA*, vol. 100, no. 21, pp. 12349–12354, Oct. 2003.

[15] A. Zafar and K.-S. Hong, "Detection and classification of three-class initial dips from prefrontal cortex," *Biomed. Opt. Exp.*, vol. 8, no. 1, pp. 367–383, 2017.

[16] J. S. Wyatt, M. Cope, D. T. Delpy, C. E. Richardson, A. D. Edwards, S. Wray, and E. O. R. Reynolds, "Quantitation of cerebral blood volume in human infants by near-infrared spectroscopy," *J. Appl. Physiol.*, vol. 68, no. 3, pp. 1086–1091, 1990.

[17] C. Matteau-Pelletier, M. Dehaes, F. Lesage, and J.-M. Lina, "$1/f$ noise in diffuse optical imaging and wavelet-based response estimation," *IEEE Trans. Med. Imag.*, vol. 28, no. 3, pp. 415–422, Mar. 2009.

[18] U. Asgher, R. Ahmad, N. Naseer, Y. Ayaz, M. J. Khan, and M. K. Amjad, "Assessment and classification of mental workload in the prefrontal cortex (PFC) using fixed-value modified Beer-Lambert law," *IEEE Access*, vol. 7, pp. 143250–143262, 2019.

[19] T. K. K. Ho, J. Gwak, C. M. Park, and J.-I. Song, "Discrimination of mental workload levels from multi-channel fNIRS using deep leaning-based approaches," *IEEE Access*, vol. 7, pp. 24392–24403, 2019.

[20] S. Fantini, M. A. Franceschini, J. B. Fishkin, B. Barbieri, and E. Gratton, "Quantitative-determination of the absorption-spectra of chromophores in strongly scattering media: A light-emitting-diode based technique," *Appl. Opt.*, vol. 33, no. 22, pp. 5204–5213, 1994.

[21] G. Gratton, M. Fabiani, D. Friedman, M. A. Franceschini, S. Fantini, P. Corballis, and E. Gratton, "Rapid changes of optical-parameters in the human brain during a tapping task," *J. Cognit. Neurosci.*, vol. 7, no. 4, pp. 446–456, 1995.

[22] S. Fantini, D. Hueber, M. A. Franceschini, E. Gratton, W. Rosenfeld, P. G. Stubblefield, D. Maulik, and M. R. Stankovic, "Non-invasive optical monitoring of the newborn piglet brain using continuous-wave and frequency-domain spectroscopy," *Phys. Med. Biol.*, vol. 44, no. 6, pp. 1543–1563, Jun. 1999.

[23] A. Torricelli, D. Contini, A. Pifferi, M. Caffini, R. Re, L. Zucchelli, and L. Spinelli, "Time domain functional NIRS imaging for human brain mapping," *NeuroImage*, vol. 85, pp. 28–50, Jan. 2014.

[24] Z. Wang, D. Ming, Y. Zhou, L. Chen, B. Gu, W. Yi, S. Liu, M. Xu, H. Qi, and F. He, "BCI monitor enhances electroencephalographic and cerebral hemodynamic activations during motor training," *IEEE Trans. Neural Syst. Rehabil. Eng.*, vol. 27, no. 4, pp. 780–787, Apr 2019.

[25] A. Aarabi, V. Osharina, and F. Wallois, "Effect of confounding variables on hemodynamic response function estimation using averaging and deconvolution analysis: An event-related NIRS study," *NeuroImage*, vol. 155, pp. 25–49, 2017.

[26] A. Shah and A.-K. Seghouane, "An integrated framework for joint HRF and drift estimation and HbO/HbR signal improvement in fNIRS data," *IEEE Trans. Med. Imag.*, vol. 33, no. 11, pp. 2086–2097, Nov. 2014.

[27] X.-S. Hu, K.-S. Hong, S. S. Ge, and M.-Y. Jeong, "Kalman estimator- and general linear model-based on-line brain activation mapping by near-infrared spectroscopy," *Biomed. Eng. OnLine*, vol. 9, no. 1, p. 82, 2010.

[28] D. A. Boas, A. M. Dale, and M. A. Franceschini, "Diffuse optical imaging of brain activation: Approaches to optimizing image sensitivity, resolution, and accuracy," *NeuroImage*, vol. 23, pp. S275–S288, Jan. 2004.

[29] H. D. Nguyen and K.-S. Hong, "Bundled-optode implementation for 3D imaging in functional near-infrared spectroscopy," *Biomed. Opt. Exp.*, vol. 7, no. 9, pp. 3491–3507, 2016.

[30] K.-S. Hong and A. Zafar, "Existence of initial dip for BCI: An illusion or reality," *Frontiers Neurorobot.*, vol. 12, Oct. 2018, Art. no. 69.

[31] D. A. Benaron, C. D. Kurth, J. M. Steven, M. Delivoria-Papadopoulos, and B. Chance, "Transcranial optical path length in infants by near-infrared phase-shift spectroscopy," *J. Clin. Monitor.*, vol. 11, no. 2, pp. 109–117, Mar. 1995.

[32] H. Zhao, Y. Tanikawa, F. Gao, Y. Onodera, A. Sassaroli, K. Tanaka, and Y. Yamada, "Maps of optical differential pathlength factor of human adult forehead, somatosensory motor and occipital regions at multi-wavelengths in NIR," *Phys. Med. Biol.*, vol. 47, no. 12, pp. 2075–2093, Jun. 2002.

[33] T. Talukdar, J. H. Moore, and S. G. Diamond, "Continuous correction of differential path length factor in near-infrared spectroscopy," *J. Biomed. Opt.*, vol. 18, no. 5, May 2013, Art. no. 056001.

[34] D. T. Delpy, M. Cope, P. V. D. Zee, S. Arridge, S. Wray, and J. Wyatt, "Estimation of optical pathlength through tissue from direct time of flight measurement," *Phys. Med. Biol.*, vol. 33, no. 12, pp. 1433–1442, Dec. 1988.

[35] S. Chatterjee, J. P. Phillips, and P. A. Kyriacou, "Differential pathlength factor estimation for brain-like tissue from a single-layer Monte Carlo model," in *Proc. 37th Annu. Int. Conf. IEEE Eng. Med. Biol. Soc. (EMBC)*, Aug. 2015, pp. 3279–3282.

[36] D. Contini, L. Spinelli, A. Torricelli, A. Pifferi, and R. E. D. C. R. Cubeddu, "Novel method for depth-resolved brain functional imaging by time-domain NIRS," *Proc. SPIE*, vol. 6629, Jul. 2007, Art. no. 662908.

[37] C. Habermehl, C. Schmitz, S. P. Koch, J. Mehnert, and J. Steinbrink, "Depth sensitivity in multi-distance NIRS measurements in humans," in *Proc. Biomed. Opt. 3-D Imag.*, vol. 2012, Art. no. BSu3A.84.

[38] F. Scholkmann and M. Wolf, "General equation for the differential pathlength factor of the frontal human head depending on wavelength and age," *J. Biomed. Opt.*, vol. 18, no. 10, Oct. 2013, Art. no. 105004.

[39] D. Q. Piao, R. L. Barbour, H. L. Graber, and D. C. Lee, "On the geometry dependence of differential pathlength factor for near-infrared spectroscopy. I. Steady-state with homogeneous medium," *J. Biomed. Opt.*, vol. 20, no. 10, 2015, Art. no. 105005.

[40] A. M. Chiarelli, D. Perpetuini, C. Filippini, D. Cardone, and A. Merla, "Differential pathlength factor in continuous wave functional near-infrared spectroscopy: Reducing hemoglobin's cross talk in high-density recordings," *Neurophotonics*, vol. 6, no. 3, 2019, Art. no. 035005.
[41] D. Hueber, S. Fantini, A. Cerussi, and B. Barbieri, "New optical probe designs for absolute (self-calibrating) NIR tissue hemoglobin measurements," *Proc. SPIE*, vol. 3597, Jul. 1999, pp. 618–631.
[42] H. W. Zhang, J. W. Xie, J. A. Ge, W. L. Lu, and B. F. Zong, "Adaptive strong tracking square-root cubature Kalman filter for maneuvering aircraft tracking," *IEEE Access*, vol. 6, pp. 10052–10061, 2018.
[43] B. Han, H. Huang, L. Lei, C. Huang, and Z. Zhang, "An improved IMM algorithm based on STSRCKF for maneuvering target tracking," *IEEE Access*, vol. 7, pp. 57795–57804, 2019.
[44] L. Zhao, J. Wang, T. Yu, H. Jian, and T. Liu, "Design of adaptive robust square-root cubature Kalman filter with noise statistic estimator," *Appl. Math. Comput.*, vol. 256, pp. 352–367, Apr. 2015.
[45] I. Arasaratnam and S. Haykin, "Cubature Kalman filters," *IEEE Trans. Autom. Control*, vol. 54, no. 6, pp. 1254–1269, Jun. 2009.
[46] M. Pramanik, A. Routray, and P. Mitra, "Accurate real-time estimation of power system transients using constrained symmetric strong tracking square-root cubature Kalman filter," *IEEE Access*, vol. 7, pp. 165692–165709, 2019.
[47] K.-S. Hong and P.-T. Pham, "Control of axially moving systems: A review," *Int. J. Control, Autom. Syst.*, vol. 17, no. 12, pp. 2983–3008, Dec. 2019.
[48] A. K. Pamosoaji, M. Piao, and K.-S. Hong, "PSO-based minimum-time motion planning for multiple vehicles under acceleration and velocity limitations," *Int. J. Control, Autom. Syst.*, vol. 17, no. 10, pp. 2610–2623, Oct. 2019.
[49] E. A. Wan and A. T. Nelson, "Dual extended Kalman filter methods," in *Kalman Filtering and Neural Networks*, S. Haykin, Ed. Hoboken, NJ, USA: Wiley, 2001, pp. 123–173.
[50] R.-C. Dong, Q.-J. Guo, W. Yuan, W. Du, X.-H. Yang, and Y.-J. Zhao, "The finite element model of seated whole human body for vibration investigations of lumbar spine in complex system," *IEEE Access*, vol. 8, pp. 125046–125055, 2020.
[51] R. Y. Li, W. Y. Yang, and H. M. Liang, "Multi-physics finite element model of relay contact resistance and temperature rise considering multi-scale and 3D fractal surface," *IEEE Access*, vol. 8, pp. 122241–122250, 2020.
[52] M. Boureghda and T. Bouden, "A deconvolution scheme for the stochastic metabolic/hemodynamic model (sMHM) based on the square root cubature Kalman filter and maximum likelihood estimation," *Biomed. Signal Process. Control*, vol. 45, pp. 284–304, Aug. 2018.
[53] R. B. Buxton, K. Uludağ, D. J. Dubowitz, and T. T. Liu, "Modeling the hemodynamic response to brain activation," *NeuroImage*, vol. 23, pp. S220–S233, Jan. 2004.
[54] T. Deneux and O. Faugeras, "Using nonlinear models in fMRI data analysis: Model selection and activation detection," *NeuroImage*, vol. 32, no. 4, pp. 1669–1689, Oct. 2006.
[55] S. Zhao, Y. Cui, L. Huang, L. Xie, Y. Chen, J. Han, L. Guo, S. Zhang, T. Liu, and J. Lv, "Supervised brain network learning based on deep recurrent neural networks," *IEEE Access*, vol. 8, pp. 69967–69978, 2020.
[56] H. Dehghani, M. E. Eames, P. K. Yalavarthy, S. C. Davis, S. Srinivasan, C. M. Carpenter, B. W. Pogue, and K. D. Paulsen, "Near infrared optical tomography using NIRFAST: Algorithm for numerical model and image reconstruction," *Commun. Numer. Methods Eng.*, vol. 25, no. 6, pp. 711–732, Jun. 2009.
[57] S.-H. Kim and H.-L. Choi, "Convolutional neural network for monocular vision-based multi-target tracking," *Int. J. Control, Autom. Syst.*, vol. 17, no. 9, pp. 2284–2296, Sep. 2019.
[58] L. Cao, D. Ran, X. Chen, X. Li, and B. Xiao, "Huber second-order variable structure predictive filter for satellites attitude estimation," *Int. J. Control, Autom. Syst.*, vol. 17, no. 7, pp. 1781–1792, Jul. 2019.
[59] L. M. Paz, J. D. Tardos, and J. Neira, "Divide and Conquer: EKF SLAM in O(n)," *IEEE Trans. Robot.*, vol. 24, no. 5, pp. 1107–1120, Oct. 2008.
[60] A. Valade, P. Acco, P. Grabolosa, and J. Y. Fourniols, "A study about Kalman filters applied to embedded sensors," *Sensors*, vol. 17, no. 12, p. 2810, 2017.

RUISEN HUANG (Graduate Student Member, IEEE) received the B.S. and M.S. degrees in electrical engineering from Southwest Jiaotong University, Chengdu, Sichuan, China, in 2014 and 2017, respectively, and the Diploma degree in engineering from the École Centrale Paris, CentraleSupélec, Paris-Saclay, France, in 2017. He is currently pursuing the Ph.D. degree with the School of Mechanical Engineering, Pusan National University, Busan, South Korea. His research interests include brain signal processing, brain–computer interface, and machine learning.

KEUM-SHIK HONG (Fellow, IEEE) received the B.S. degree in mechanical design and production engineering from Seoul National University, in 1979, the M.S. degree in mechanical engineering from Columbia University, New York, in 1987, and the M.S. degree in applied mathematics and the Ph.D. degree in mechanical engineering from the University of Illinois at Urbana–Champaign, in 1991. He joined the School of Mechanical Engineering, Pusan National University (PNU), in 1993. His Integrated Dynamics and Control Engineering Laboratory was designated a National Research Laboratory by the Ministry of Science and Technology, South Korea, in 2003. In 2009, under the auspices of the World Class University Program, Ministry of Education, Science, and Technology, South Korea, he established the Department of Cogno-Mechatronics Engineering, PNU.

Dr. Hong was the past President of the Institute of Control, Robotics and Systems (ICROS), South Korea. He is the President of the Asian Control Association. He is a Fellow of the Korean Academy of Science and Technology, an ICROS Fellow, a member of the National Academy of Engineering of South Korea and many other societies. He was the Organizing Chair of the ICROS-SICE International Joint Conference 2009, Fukuoka, Japan. He served as an Associate Editor for *Automatica* from 2000 to 2006 and the Editor-in-Chief for the *Journal of Mechanical Science and Technology* from 2008 to 2011. He is serving as the Editor-in-Chief for the *International Journal of Control, Automation, and Systems*.

His current research interests include brain–computer interface, nonlinear systems theory, adaptive control, distributed parameter systems, autonomous vehicles, and innovative control applications in brain engineering. He has received many awards, including the Best Paper Award from the KFSTS of South Korea in 1999, the F. Harashima Mechatronics Award in 2003, the IJCAS Scientific Activity Award in 2004, the Automatica Certificate of Outstanding Service in 2006, the Presidential Award of South Korea in 2007, the ICROS Achievement Award in 2009, the IJCAS Contribution Award in 2010, the Premier Professor Award in 2011, the JMST Contribution Award in 2011, the IJCAS Contribution Award in 2011, the IEEE Academic Award in 2016, and the IJCAS Contribution Award in 2020.